Supplemental Material: Spin and Charge Fluctuation Induced Pairing in ABCB Tetralayer Graphene

Ammon Fischer,[1,*] Lennart Klebl,[2,*] Jonas B. Hauck,[1] Alexander Rothstein,[3,4] Lutz Waldecker,[3] Bernd Beschoten,[3] Tim O. Wehling,[2,5] and Dante M. Kennes[1,6,†]

[1]*Institute for Theory of Statistical Physics, RWTH Aachen University, and JARA Fundamentals of Future Information Technology, 52062 Aachen, Germany*
[2]*I. Institute for Theoretical Physics, Universität Hamburg, Notkestraße 9-11, 22607 Hamburg, Germany*
[3]*2nd Institute of Physics and JARA-FIT, RWTH Aachen University, 52074 Aachen, Germany*
[4]*Peter Grünberg Institute (PGI-9), Forschungszentrum Jülich, 52425 Jülich, Germany*
[5]*The Hamburg Centre for Ultrafast Imaging, 22761 Hamburg, Germany*
[6]*Max Planck Institute for the Structure and Dynamics of Matter, Center for Free Electron Laser Science, 22761 Hamburg, Germany*

(Dated: October 20, 2023)

S1. NON-INTERACTING HAMILTONIAN

Our tight binding Hamiltonian for graphene tetralayers is a modified Slonzecewski-Weiss-McClure (SWMC) Hamiltonian, with parameters chosen based on Ref.[43] summarized in Table SI. The Hamilton matrix can be constructed as

$$H^{y}_{i,j}(\boldsymbol{k}) = \delta_{i,j}\delta_{i,A}\Delta_y + \sum_{u_1,u_2\in\mathbb{Z}}\sum_{n}\delta_{d^{u_1,u_2}_{i,j},d_n}\, e^{-i\boldsymbol{k}\boldsymbol{R}(u_1,u_2)}\gamma_n\,, \tag{S1}$$

where i and j are site indices within the unit cell, y marks the type of the lattice and is either ABAB, ABCA or ABCB and $\delta_{i,A}$ is one if i is an a-site and 0 otherwise. u_1 and u_2 iterate over all unit cells in the infinite lattice, $\boldsymbol{R}(u_1,u_2)$ gives the vectorial distance between the unit cells and $d^{u_1,u_2}_{i,j}$ gives the distance between site i and the image of site j shifted by u_1 and u_2 unit-cell vectors.

TABLE SI. Slonzecewski-Weiss-McClure Hamiltonian model parameters.

Name	Value in eV	Distance in Å
γ_0	2.553	1.42
γ_1	0.343	3.35
γ_2	−0.009	6.70
γ_3	0.18	4.16
γ_4	0.173	3.64
γ_5	0.018	6.85
Δ_{ABAB}	−0.003	0.0, a site
Δ_{ABCA}	0.0	0.0, a site
Δ_{ABCB}	−0.018	0.0, a site

S2. RANDOM PHASE APPROXIMATION

To calculate the non-interacting susceptibility $\hat{\chi}_0(\boldsymbol{q})$ in static approximation, we must carry out the summation

$$\begin{aligned}\chi_0^{oo'}(\boldsymbol{q}) &= -\left(\lim_{iq_0\to 0}\mathrm{Tr}_k\left[\hat{G}(k-q)\odot\hat{G}(k)^T\right]\right)_{oo'}\\ &= -\frac{1}{N_{\boldsymbol{k}}}\sum_{\boldsymbol{k},b,b'}\frac{n_F(\epsilon_b(\boldsymbol{k}))-n_F(\epsilon_{b'}(\boldsymbol{k}-\boldsymbol{q}))}{\epsilon_b(\boldsymbol{k})-\epsilon_{b'}(\boldsymbol{k}-\boldsymbol{q})}\,u_{ob}(\boldsymbol{k})u^*_{o'b}(\boldsymbol{k})u^*_{ob'}(\boldsymbol{k}-\boldsymbol{q})u_{o'b'}(\boldsymbol{k}-\boldsymbol{q})\,,\end{aligned} \tag{S2}$$

where $\epsilon_b(\boldsymbol{k})$ denotes the dispersion relation and $u_{ob}(\boldsymbol{k})$ the Bloch function at momentum $\boldsymbol{k}$ for band b and orbital (site) o. In the actual numerical implementation, we make use of the fact that the only momenta $\boldsymbol{q}$ relevant for magnetic instabilities are those where $\boldsymbol{q} \approx \boldsymbol{k}_F \pm \boldsymbol{k}'_F$, with $\boldsymbol{k}_F^{(\prime)}$ on the Fermi surface. We thus choose an energy widow $W \gg T$ (in our calculation $W = 3\,\mathrm{meV}$ and $T = 0.025 \ldots 0.1\,\mathrm{meV}$) and obtain all momenta $\boldsymbol{q} \in \{\boldsymbol{k} \pm \boldsymbol{k}' \text{ with } \boldsymbol{k}, \boldsymbol{k}' \in \mathbb{FS}_W\}$ for the extended Fermi surface $\mathbb{FS}_W = \{\boldsymbol{k} \in \mathbb{BZ} \text{ s.t. } \exists b \text{ with } |\epsilon_b(\boldsymbol{k}) - \mu| < W\}$. The calculation of $\hat{\chi}_0(\boldsymbol{q})$ is perfectly parallel in $\boldsymbol{q}$. Moreover, we parallelize the summation over $\boldsymbol{k}$ to obtain higher performance in our custom CUDA kernels. We additionally note that we make use of a cached dispersion relation and obrital to band transform on a fixed momentum mesh (we checked 4800×4800 and 7200×7200 points).

From the free electronic susceptibility $\hat{\chi}_0(\boldsymbol{q})$ on the relevant $\boldsymbol{q}$, we calculate the critical on-site interaction strength required for the onset of magnetic order. The crossed particle-hole channel RPA resummation of the effective interaction yields

$$\hat{W}(\boldsymbol{q}) = \frac{\hat{U}}{\mathbb{1} - \hat{U}\,\hat{\chi}_0(\boldsymbol{q})}\,, \tag{S3}$$

where we directly observe that for an on-site Hubbard interaction $\hat{U} = U\mathbb{1}$, the maximum eigenvalue of $\hat{\chi}_0(\boldsymbol{q})$ over all $\boldsymbol{q}$ determines (i) the critical interaction strength $U_\mathrm{c} = 1/\chi_0^m(\boldsymbol{q}^m)$ and (ii) the type of magnetic order via the corresponding eigenvector $\vec{\chi}_0^m(\boldsymbol{q}^m)$.

A. Flowing random phase approximation

An alternative way to look at the RPA from above is via a single-channel functional renormalization group (FRG) flow. From the diagrams contained in the two particle irreducible flow with neglected self-energies[68] it is evident that the effective FRG vertex in static approximation sums up all diagrams contained in the effective RPA vertex Eq. (S3) when restricted to the crossed particle hole channel. We therefore rewrite the RPA as a single channel FRG, i.e.,

$$\dot{\hat{W}}_\Lambda(\boldsymbol{q}) = -\hat{W}_\Lambda(\boldsymbol{q})\dot{\hat{L}}_\Lambda(\boldsymbol{q})\hat{W}_\Lambda(\boldsymbol{q})\,. \tag{S4}$$

One quickly verifies that the solution to this differential equation is given by

$$\hat{W}_\Lambda(\boldsymbol{q}) = \frac{\hat{W}_\infty(\boldsymbol{q})}{\mathbb{1} - \hat{W}_\infty(\boldsymbol{q}) \int_\Lambda^\infty \mathrm{d}\Lambda' \dot{\hat{L}}_{\Lambda'}(\boldsymbol{q})}\,. \tag{S5}$$

From the FRG perspective, it is therefore sufficient to calculate the particle-hole loop integral to get an expression for the free susceptibility at scale T:

$$\hat{\chi}_T^\mathrm{FRG}(\boldsymbol{q}) = \int_T^\infty \mathrm{d}\Lambda\, \dot{\hat{L}}_\Lambda(\boldsymbol{q}) = \int_T^\infty \frac{\mathrm{d}\Lambda}{2\pi}\left[\frac{1}{N_{\boldsymbol{k}}}\sum_{\boldsymbol{k}} \hat{G}(i\Lambda, \boldsymbol{k}) \odot \hat{G}^T(i\Lambda, \boldsymbol{k} - \boldsymbol{q}) + \mathrm{h.c.}\right]. \tag{S6}$$

Note that we employ a sharp frequency cutoff here. $\hat{\chi}_T^\mathrm{FRG}(\boldsymbol{q})$ resembles an approximation to the Matsubara summation in the explicit RPA, where the frequencies above the lowest one are treated as continuum. Such an approximation is similar to the explicit Matsubara summation used in large unit cell systems in Ref.[49]. We observe that in the flowing RPA formulation, though, we can make use of fast Fourier transforms (FFTs) to calculate the convolution over $\boldsymbol{k}$ and $\boldsymbol{q}$. For large momentum meshes, the numerical scaling of this operation is $\mathcal{O}(N_{\boldsymbol{k}} \log N_{\boldsymbol{k}})$ instead of $\mathcal{O}(N_{\boldsymbol{k}} N_{\boldsymbol{q}})$ for the explicit sum over $\boldsymbol{k}$ for each $\boldsymbol{q}$. Using the flowing RPA trick with FFTs allows us to bump the momentum resolutions significantly higher than using the explicit RPA: We calculated the flowing RPA susceptibilities for a momentum resolution of $N_{\boldsymbol{k}} = 12288^2 = (2^{12} \cdot 3)^2$ points and confirmed that indeed our calculations are converged. Note that numerically, the flowing RPA covering roughly 400 adaptively chosen points in the Λ integral were *significantly faster* on a single CPU node of the JURECA cluster[67] than the explicit RPA CUDA kernels on four NVIDIA A100 GPUs with approximately half the resolution ($N_{\boldsymbol{k}} = 7200^2$).

B. Magnetic instabilities for other parameters

To confirm that the conduction band physics is qualitatively equivalent the effects in the valence band, we show the magnetic instabilities for both sides at $T = 10^{-4}\,\mathrm{eV}$ in Fig. S1.

The behavior of $\hat{\chi}_0(\boldsymbol{q})$ as a function of temperature is depicted in Fig. S2. Note that we include high resolution, low temperature calculations that were obtained with the *flowing RPA* trick presented in Section S2 A in panels (d,e).

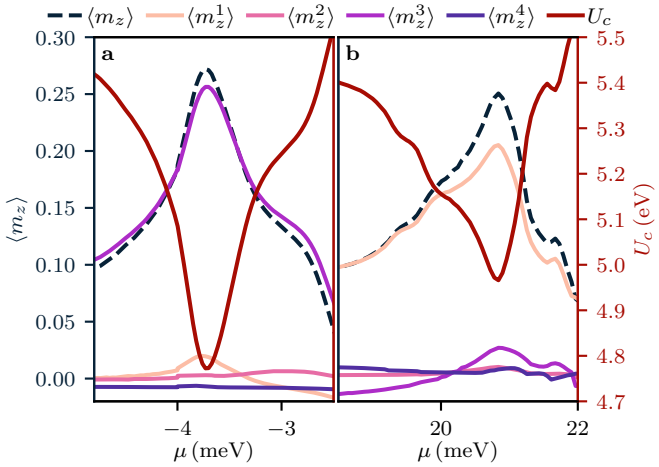

FIG. S1. Critical interaction strength (red) and layer magnetization curves for the hole-doped (a) and electron-doped (b) van Hove singularity in ABCB graphene. In contrast to the hole-doped side, the electron-doped carries most magnetization in layer A (1). Apart from that, the qualitative features are equivalent. The dominant ferrimagnetism in layer 1 [panel (a)] corresponds to the layer polarization of the Bloch functions being mostly in layer 1 (cf. Fig. 1).

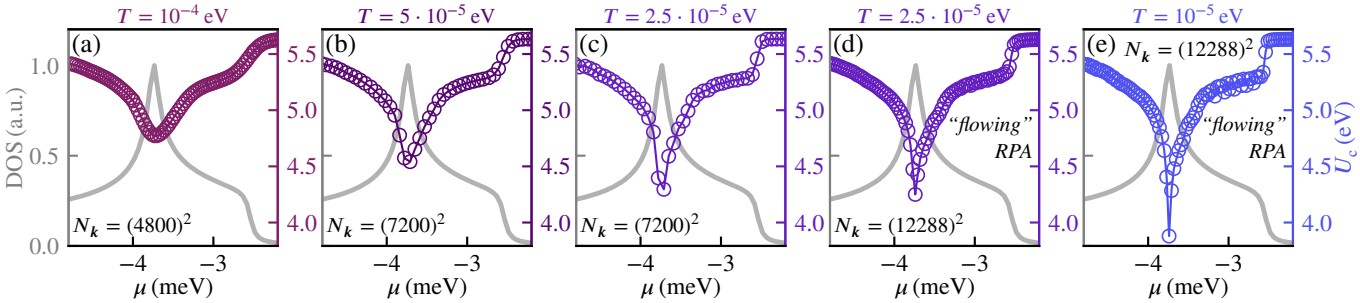

FIG. S2. Critical interaction strength as a function of filling for a range of temperatures and momentum resolutions. Panels (a-c) use the explicit RPA summations and panels (d,e) the flowing RPA.

S3. SUPERCONDUCTIVITY

To study unconventional superconductivity driven by electronic interactions, we study different mechanisms that are based on (i) spin-fluctuations by local interactions (xRPA) (ii) charge-fluctuations due to screening of the long-ranged Coulomb interactions (xdRPA) and (iii) a combined approach (dRPA) that captures a superset of diagrams contained in the mechanisms above. This section is denoted to show the corresponding diagrams describing the contributions of either mechanism to superconducting pairing and discuss their practical implementation.

A. Local Interactions

In the vicinity of magnetic instabilities, spin and charge fluctuations that are driven by local Hubbard-U interactions can provide the pairing glue for an unconventional superconducting state. To capture the effect of spin-fluctuation induced pairing in ABCB, we resort to the well-known diagrammatic expansion[56,69] based on transversal and longitudinal spin-fluctuations as shown in Figure S4. Even though orbital degrees of freedoms are not explicitly shown in the diagrams, we keep the full orbital dependence of the susceptibility and the respective interactions throughout this work. Within this approach we capture all diagrams from the exchange channel (transversal spin-fluctuations) and the subgroup of diagrams in the direct particle-hole channel that contain an even number of loops (longitudinal spin-fluctuations). As we assume the system to be in the paramagnetic phase, i.e. the normal-state Hamiltonian is $SU(2)$ symmetric, the susceptibilities carry no explicit spin degree of freedom and it is possible to only consider the pairing vertex, where the ingoing- and outgoing spins are opposite. All spin-singlet (spin-triplet) instabilities are then captured in the anti-symmetric (symmetric) sector of the pairing vertex. The transversal and longitudinal spin-fluctuation

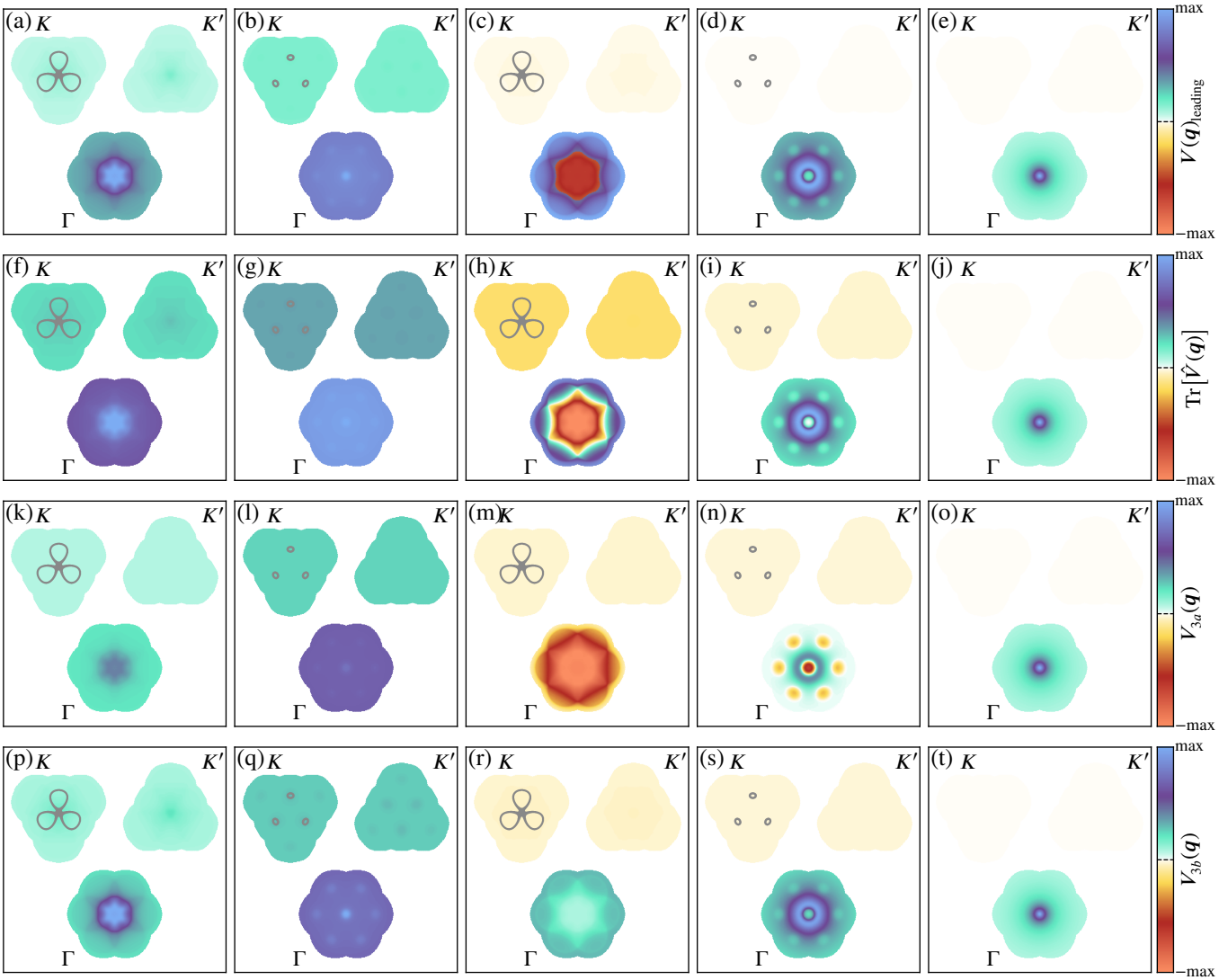

FIG. S3. Momentum and orbital structure of effective vertices. First column: xRPA vertex for $\mu \approx \mu_{\text{VHS}}$, second column: xRPA vertex for μ at the valence band edge, third column: dRPA vertex for $\mu \approx \mu_{\text{VHS}}$, fourth column: dRPA vertex for μ at the valence band edge, and fifth column: bare Ohno vertex. We display the leading vertex eigenvalue in the first row (a-e), the trace over the orbitals in the second row (f-j), the projection of the vertex to the a-site of the C layer (layer 3) in the third row (k-o), and the projection to the b-site of the C layer (layer 3) in the fourth row (p-t). The colorbar in each panel is normalized individually, with panels (k,p), (l,q), (m,r), (n,s), and (o,t) each sharing the normalization. In the orbital projections we observe that attraction is generated only on the a-site of layer 3, such that it is projected out by the particle-particle loop in the linearized gap equation Eq. (S12) and the effective vertex relevant for superconductivity remains repulsive in momentum space. In the subpanels around the K point, we additionally include the Fermi contour for scale.

diagrams translate to

$$\left[V_X^{\text{PP}}\right]_{o_1o_2o_3o_4}(\boldsymbol{k},\boldsymbol{k}') = U\delta_{o_1,o_2}\delta_{o_3,o_4}\delta_{o_1,o_4} + \left[\frac{U^2\hat{\chi}_0(\boldsymbol{k}+\boldsymbol{k}')}{1-U\hat{\chi}_0(\boldsymbol{k}+\boldsymbol{k}')}\right]_{o_1,o_2}\delta_{o_1,o_4}\delta_{o_2,o_3} + \left[\frac{U^3\hat{\chi}_0(\boldsymbol{k}-\boldsymbol{k}')^2}{1-U^2\hat{\chi}_0(\boldsymbol{k}-\boldsymbol{k}')^2}\right]_{o_1,o_2}\delta_{o_1,o_3}\delta_{o_2,o_4}. \quad \text{(S7)}$$

The effective spin fluctuation vertex Eq. (S7) is proportional to $(1-U\chi_0)^{-1}$ reminiscent of the magnetic instability that is reached when the Stoner condition at $U \to U_c$ is met. For $U \geq U_c$ the theory hence breaks down as magnetic fluctuations diverge and the system orders magnetically. To avoid numerical instabilities when calculating superconducting gap functions using the effective pairing vertex V_C^{PP}, we perform the matrix inversions $1/(1-U\chi_0)$ and $1/(1-U^2(\chi_0)^2)$ in Eq. (S7) in the eigenspace of χ_0 and add a small imaginary broadening constant $i\,\eta_{\text{FLEX}} = 50\,\text{meV}$ to all the eigenvalues in the denominator. Note that the energy scale of this broadening constant is to be compared with (and has to be very small in regard to) the *vertex* energy scales, i.e. $4-5\,\text{eV}$ and *not the valley-flat band* energy scales.

As explained in the main text, local interactions are flat in momentum space such that both inter- and intravalley coupling are present. In conjunction with single layer ferromagnetic fluctuations, the intervalley exchange enhances order parameters that are (i) spin-triplet and (ii) change sign under a valley flip. We find that local interactions exclusively promote valley-singlet, spin-triplet f-wave order for all fillings around the VHS in ABCB stacked graphene. We can understand the prevailance of f-wave superconductivity from a miscroscopic picture when analyzing the effective vertex structure Eq. (S7) as shown in Figure S3. As known from the one-band Hubbard model[69] the spin fluctuation vertex remains purely positive in momentum space such that the symmetry of the superconducting order parameter must exhibit a sign change at the respective Fermi surface. We note that even though the effective vertex peaks around Γ, see Figure S3 (a,b and subsequent columns), the effective vertex has substantial amplitude for momentum transfers that connect the two valleys $K^{(\prime)}$. Therefore, the superconducting condensate can minimize its free energy by changing sign between the valleys leading to dominante f-wave SC order. At the same time, the sub-leading instability within the xRPA is of $p_{x,y}$-wave type, see Figure 4 (b) in the main text. The $p_{x,y}$ spin-triplet instability is an anti-symmetric basis function of the E irreducible representation of C_{3v} in momentum space. Similar to the dRPA results, the $p_{x,y}$-wave is driven by fluctuations that are centered at Γ. We hence note that the delicate interplay of short and long-ranged interactions, which we resolve within our orbital-resolved RPA, drive either order parameter.

B. Long-Ranged Interactions

Pairing mediated by screened Coulomb interactions can be accounted for by the effective pairing vertex

$$\left[V_D^{\mathrm{PP}}\right]_{o_1o_2o_3o_4}(\boldsymbol{k},\boldsymbol{k}') = \left[\hat{V}^O(\boldsymbol{k}-\boldsymbol{k}')\frac{1}{\mathbb{1}+2\hat{\chi}_0(\boldsymbol{k}-\boldsymbol{k}')\hat{V}^O(\boldsymbol{k}-\boldsymbol{k}')}\right]_{o_1o_2}\delta_{o_1o_3}\delta_{o_2o_4}, \tag{S8}$$

where $\hat{V}^O(\boldsymbol{q}) = V^O_{o_1o_2}(\boldsymbol{q})$ is the Fourier transform of the full Coulomb interaction and the factor of 2 in the denominator arises due to the internal trace over spin indices in the direct particle-hole channel. The latter is a direct consequence of the $SU(2)$ symmetry in the normal-state Hamiltonian. As described in the main text, we use a realistic (orbital-resolved) "Ohno" interaction profile[51,63]

$$V^O(\boldsymbol{r}) = \frac{Ua}{\sqrt{a^2+\boldsymbol{r}^2}}e^{-|\boldsymbol{r}|/d}, \tag{S9}$$

with realistic parameters $a = 0.3a_0$ and $d = 200a_0$ (where $a_0 = 2.46$ Å is the graphene lattice constant). The parameter d controls the external screening from, e.g., metallic gates or the substrate, a controls the atomic scale decay of the Coulomb interaction in real space, and U sets the on-site (Hubbard) interaction strength. In particular, the 'Ohno" interaction profile ensures consistent treatment of long- and short-ranged terms of the Coulomb interaction. We further checked that our results do not change when varying the screening parameter in the realistic range of $d = 50\ldots 200a_0$, see Section S3 E.

As argued in the main text, order parameters with an intravalley sign change are generically favored by the screened Coulomb interaction for realistic interaction parameters as screening induced pairing Eq. (4) is most relevant for momenta $\boldsymbol{q}_D$ where the polarization function $\hat{\chi}_0(\boldsymbol{q}_D)$ peaks. To underline this argument, we show the momentum structure of the effective pairing vertex mediated by screened Coulomb interactions in Figure S3. Indeed, we observe that opposite to the xRPA approach no amplitude exists at momentum transfers $\boldsymbol{q}_D = K^{(\prime)}$ that connects the two valley.

C. Combined mechanism for long- and short-ranged interactions

Due to the different orbital- and momentum structures in the exchange and direct particle-hole channel, it is in general not possible to resum long-ranged interactions in the former channel. This is because the Fourier transform of the Ohno interaction $V^O_{o_1o_2}(\boldsymbol{q}_D)$ carries a channel-specific transfer momentum $\boldsymbol{q}_D = \boldsymbol{k}-\boldsymbol{k}'$ which is native in the direct particle-hole channel (each interaction line in Figure S4 carries transfer momentum $\boldsymbol{q}$), but non-native in the exchange channel. Eq. (S7) shows that the native momentum transfer in the exchange channel is $\boldsymbol{q}_C = \boldsymbol{k}+\boldsymbol{k}'$ such that a simple RPA-like resummation with a single momentum transfer can no longer be achieved. In fact, it becomes necessary to unravel the full momentum and orbital dependence of the initial vertex and the susceptibilites, i.e. compute and store $V^O_{o_1o_2o_3o_4}(\boldsymbol{k},\boldsymbol{k}',\boldsymbol{q})$ and $\chi^0_{o_1o_2o_3o_4}(\boldsymbol{k},\boldsymbol{q})$. To resolve the small Fermi surface patches in multilayer graphene systems, we sample the entire BZ with $N_{\boldsymbol{k}} = 7200^2$ point and it hence becomes numerically unfeasible to obtain the effective pairing vertex. Therefore, we propose an alternative approach which only accounts for local interactions in the exchange channel and takes the full long-ranged interaction in the direct particle-hole channel, i.e. the best of the previous approaches that can be handled numerically.

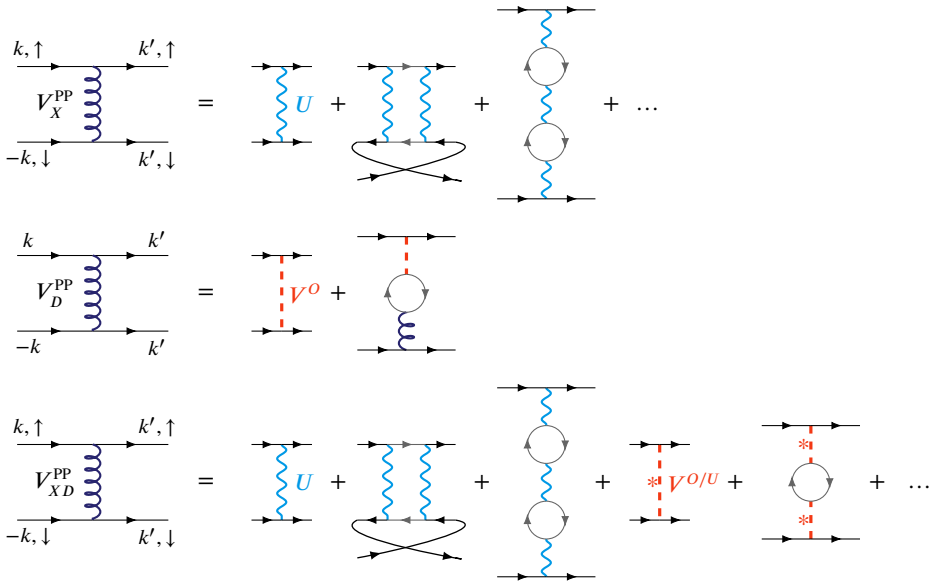

FIG. S4. Diagrams contributing to the effective pairing vertex for different mechanims within the random phase approximations (RPA). The effective scattering vertex for Cooper pairs with momenta $(\boldsymbol{k}, -\boldsymbol{k})$ and opposite spins for xRPA (upper row), dRPA (middle row) and xdRPA (lower row). Blue interaction lines indicate local Hubbard interactions, whereas the red interaction contains the full long-ranged (screened) Coulomb interaction with the Fourier transform $V^O(\boldsymbol{q})$ of the Ohno interaction profile Eq. (3). The xRPA picks up contributions from the exchange as well as the direct particle-hole channel that contains an even number of loops between the in- and out-going legs. The xdRPA contains all diagrams from the V_X^{PP} vertex, but additionally resums the long-ranged Coulomb interaction in the direct particle-hole channel. As we only consider scattering of Cooper pairs with opposite spin, the local interaction must be removed from the full Coulomb interaction $V^{O/U}$ in order to preserve the spin configuration of the effective vertex V_{XD}^{PP}. All diagramatic contributions are resummed to infinite order in the bare interactions, which is denoted by the dots or the self-consistent formulation of diagrams, respectively.

As local interactions are accounted for in the exchange channel only, their contribution can be simply ported from the xRPA. For the direct particle-hole channel we would like to take the full long-ranged Coulomb interaction as in the dRPA. This can not be done trivially as we already know from the xRPA appraoch that the resummation within RPA of local interactions must be constrained such that only an even number of loops occur between the in- and out-going legs of the opposite spin vertex Eq. (S7). We can solve this problem by writing the spin-dependence of the susceptibility and the initial vertex explicitly and constrain the effective pairing vertex to the configuration $(\uparrow\downarrow\uparrow\downarrow)$ afterwards. To this end we define

$$\begin{aligned}\tilde{\chi}^{s_1 s_2}_{o_1 o_2}(\boldsymbol{q}) &= \chi^0_{o_1 o_2}(\boldsymbol{q})\delta_{s_1 s_2}\\ \tilde{V}^{s_1 s_2}_{o_1 o_2}(\boldsymbol{q}) &= V^{O/U}_{o_1 o_2}(\boldsymbol{q})\delta_{s_1 s_2} + U\delta_{s_1 \bar{s}_2},\end{aligned} \tag{S10}$$

where $V^{O/U}_{o_1 o_2}(\boldsymbol{q})$ is the Fourier transform of the Coulomb interaction, but without the local Hubbard-U term. The renormalized interaction within RPA is hence given by

$$\begin{aligned}\left[\tilde{V}^{\mathrm{PP}}_{XD}\right]^{s_1 s_2 s_1 s_2}_{o_1 o_2 o_3 o_4}(\boldsymbol{k}, \boldsymbol{k}') &= \left[\hat{\tilde{V}}(\boldsymbol{k}-\boldsymbol{k}')\frac{1}{\mathbb{1} + \hat{\tilde{\chi}}(\boldsymbol{k}-\boldsymbol{k}')\hat{\tilde{V}}(\boldsymbol{k}-\boldsymbol{k}')}\right]_{(s_1 o_1)(s_2 o_2)} \delta_{o_1 o_3}\delta_{o_2 o_4}\\ \left[V^{\mathrm{PP}}_{XD}\right]^{\uparrow\downarrow\uparrow\downarrow}_{o_1 o_2 o_3 o_4}(\boldsymbol{k}, \boldsymbol{k}') &= \left[\tilde{V}^{\mathrm{PP}}_{XD}\right]^{\uparrow\downarrow\uparrow\downarrow}_{o_1 o_2 o_3 o_4}(\boldsymbol{k}, \boldsymbol{k}') + \left[\frac{U^2\hat{\chi}_0(\boldsymbol{k}+\boldsymbol{k}')}{1 - U\hat{\chi}_0(\boldsymbol{k}+\boldsymbol{k}')}\right]_{o_1, o_2} \delta_{o_1, o_4}\delta_{o_2, o_3}\end{aligned} \tag{S11}$$

In the last step, we have restricted the vertex to the opposite spin configuration $(\uparrow\downarrow\uparrow\downarrow)$ such that we recover all terms of the direct particle-hole channel that were present in the xRPA and the dRPA.

D. Linearized gap equation

To obtain information about the pairing symmetry of the underlying Cooper pairs as well as the superconducting coupling constant, i.e. the critical temperature of the superconducting transition, we solve a linearized gap equation in the projected

subspace containing the bands in an energy window W around the Fermi level

$$\lambda_{\mathrm{SC}}\Delta_b(\boldsymbol{k}) = -\frac{1}{N_{\boldsymbol{k}}}\sum_{\boldsymbol{k}'b'}\hat{V}^{\mathrm{PP}}_{a,bb'}(\boldsymbol{k},\boldsymbol{k}')\chi^{\mathrm{PP}}_{b'}(\boldsymbol{k}')\Delta_{b'}(\boldsymbol{k}'), \quad a \in \{X, D, XD\} \tag{S12}$$

where $\hat{V}^{\mathrm{PP}}_{bb'}$ and $\chi^{\mathrm{PP}}_{b'}$ denote the band-projected effective pairing vertex and particle-particle susceptibility, respectively. The largest eigenvalue $\lambda_{\mathrm{SC}} > 0$ will lead to the highest transition temperature T_c and the corresponding eigenfunction $\Delta(\boldsymbol{k}, b)$ determines the symmetry of the gap, which can be classified according to the irreducible representations of the point group of the normal-state Hamiltonian. The band-projected quantities in Eq. (S12) are defined as

$$\hat{V}^{\mathrm{PP}}_{bb'}(\boldsymbol{k},\boldsymbol{k}') = \sum_{o_1\dots o_4} u^*_{o_1,b}(\boldsymbol{k})u^*_{o_2,b}(-\boldsymbol{k})V^{\mathrm{PP}}_{o_1,o_2,o_3,o_4}(\boldsymbol{k},\boldsymbol{k}')u_{o_3,b}(\boldsymbol{k}')u_{o_4,b}(-\boldsymbol{k}'), \tag{S13}$$

$$\chi^{\mathrm{PP}}_b(\boldsymbol{k}) = \frac{n_F(\epsilon_b(\boldsymbol{k})) - n_F(-\epsilon_b(-\boldsymbol{k}))}{\epsilon_b(\boldsymbol{k}) + \epsilon_b(-\boldsymbol{k})}. \tag{S14}$$

In ABCB, only a single band contributes to the Fermi surface on the hole-doped side in the vicinity of the VHS. Therefore, the linearized gap equation Eq. (S12) can effectively be constrained to only capture points on the Fermi surface within the respective band, i.e. only intraband pairing of electrons becomes significant. To this end, we project the effective pairing vertex from orbital to band space Eq. (S13). The vertex $\hat{V}^{\mathrm{PP}}_{bb'}(\boldsymbol{k},\boldsymbol{k}')$ hence describes scattering of Cooper pairs with momenta $(\boldsymbol{k},-\boldsymbol{k})$ on Fermi surface patch $\mathcal{S}_b$ to $(\boldsymbol{k}',-\boldsymbol{k}')$ on Fermi surface patch $\mathcal{S}_{b'}$. Moreover, we can restrict the momentum dependence of the vertex to points on the Fermi surface. In fact, the problem of setting up the pairing vertex reduces to determine proper points on the Fermi surface, i.e. momentum points that satisfy $\mu_{\mathrm{min}} < \epsilon_b(\boldsymbol{k}) < \mu_{\mathrm{max}}$. To treat this cutoff problem consistently, we choose $\mu_{\mathrm{min}} = -5$ meV and $\mu_{\mathrm{max}} = -2$ meV to capture all fillings on the hole-doped side for which we analyze the superconducting instabilities. In particular, we ensure that Fermi surface broadening may not be smaller than thermal broadening in the system: $\eta_{\mathrm{FS}} > T$. The explicit contraction of the effective pairing vertex with the particle-particle loop Eq. (S12) will suppress all contributions that are not in the immediate vicinity of the Fermi surface $\propto \epsilon^{-1}$.

E. Temperature and Screening dependence of the superconducting order parameter

In this section, we show how the superconducting instabilities discussed in the manuscript are subject to changes in temperature and the screening parameter d.

First, we study the robustness of our results when varying the screening parameter d. We note that screening of the long-ranged Coulomb interaction may in general also depend on environmental screening by e.g. metallic gates or the substrate. Our results are summarized in Figure S5, where we show the superconducting coupling constant λ_{SC} as function of the on-site Hubbard-U at $\mu = \mu_{\mathrm{VHS}}$ for different screening lengths of $d = 50a_0, 200a_0$ within the xdRPA approach. Apparently, all qualitative features remain robust when increasing the screening to $d = 50a_0 \approx 10$ nm the such that we conclude that screening of the long-ranged tail of the Coulomb interaction does not affect the formation of superconducting instabilities notably.

Next, we study the dependence of the superconducting coupling constant λ_{SC} on the temperature broadening T that enters the calculations of the particle-hole (particle-particle) susceptibilities. As electronic states are smeared in an energy window $\sim T$ around the Fermi surface due to the appearance of Fermi functions in Eq. (S2) (Eq. (S13)), this also affects the formation of magnetic order and thus the values of the superconducting coupling constant λ_{SC}. Within the xRPA approach the critical Stoner value U_c decreases with temperature as already demonstrated in Figure S2. As superconductivity mediated by spin fluctuation is enhanced by the Stoner renormalization factor $(1-U\hat{\chi}_0)^{-1}$, we observe that the SC coupling constant λ_{SC} is enhanced particularly at the VHS, where we approach the limit $U \to U_c$. At $U = 4.5$ eV, we see that for $T = 0.25$ K, we already entered the Stoner phase as λ_{SC} drops to zero, whereas at higher temperatures superconductivity prevails. Fro the dRPA we also observe a successive increase of λ_{SC} by lowering the temperature. Especially the peak close to the valence band edge is increased significantly when lowering the temperature. The behaviour of the combined xdRPA approach can be deduced from the effects of the xRPA and dRPA separately.

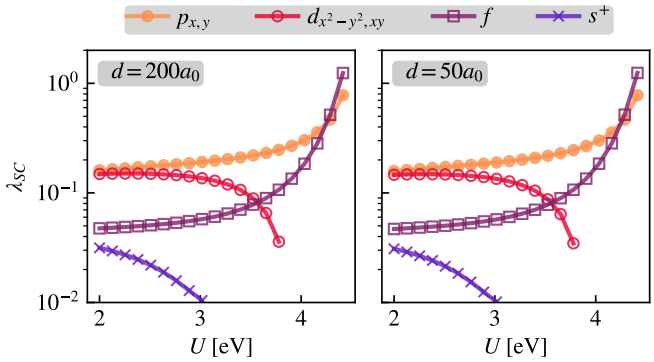

FIG. S5. Screening dependence of the superconducting order within the xdRPA mechanism. Changing the screening parameter from $d = 200a_0$ to $d = 50a_0$ leads to almost identical superconducting coupling constants λ_{SC} and leaves the symmetry of the leading SC order paramter untouched.

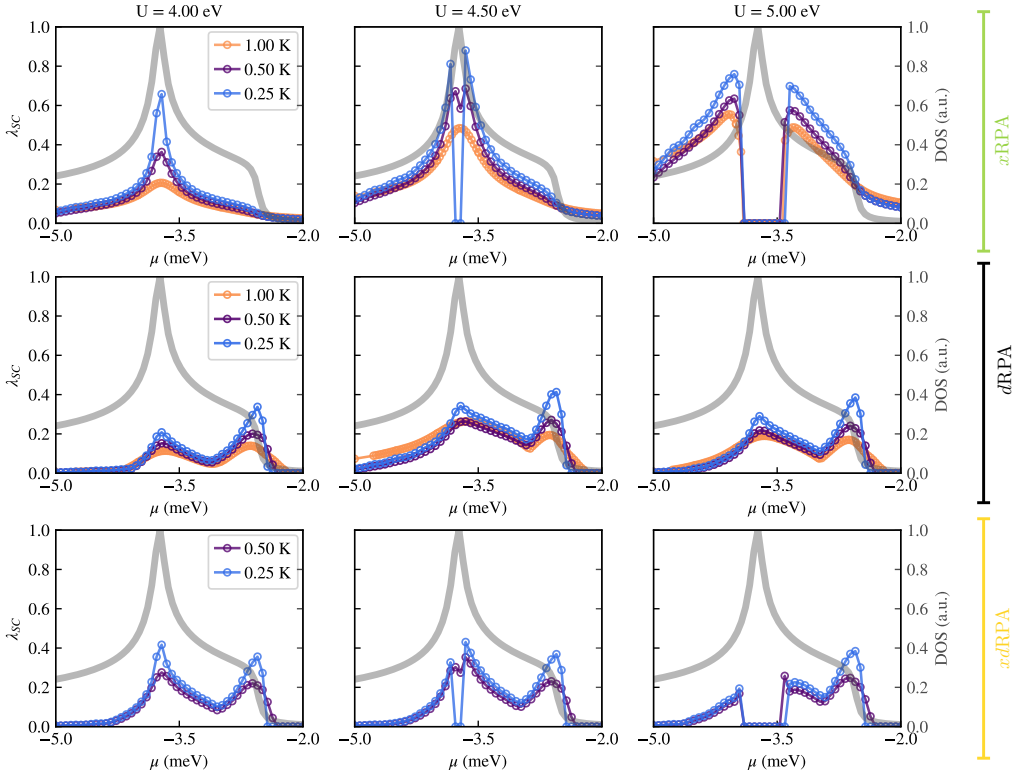

FIG. S6. Temperature dependence for the different superconducting mechanisms xRPA, dRPA and xdRPA. Each panel shows the leading superconducting coupling constant λ_{SC} as function of chemical potential μ on the hole-doped side of ABCB. Different columns display the results for different values of the local Hubbard-U interactions, whereas different rows show the different mechanisms based on spin fluctuations (xRPA), screened Coulomb interactions (dRPA) and a combined mechanisms (xdRPA) that captures both long and short ranged Coulomb interactions.